Article

Nanoporous TiN/TiO₂/Alumina Membrane for Photoelectrochemical Hydrogen Production from Sewage Water

Abdullah Almohammedi [1], Mohamed Shaban [1,*], Huda Mostafa [2] and Mohamed Rabia [2,3]

[1] Department of Physics, Faculty of Science, Islamic University in Madinah,
Al-Madinah Al-Munawarah 42351, Saudi Arabia; ard.almohammedi@hotmail.com

[2] Nanophotonics and Applications (NPA) Lab, Physics Department, Faculty of Science, Beni-Suef University,
Beni-Suef 62514, Egypt; hudamostafa55@gmail.com (H.M.); mohamedchem@science.bsu.edu.eg (M.R.)

[3] Polymer Research Laboratory, Chemistry Department, Faculty of Science, Beni-Suef University,
Beni-Suef 62511, Egypt

* Correspondence: mssfadel@aucegypt.edu

Abstract: An aluminum oxide, Al_2O_3, template is prepared using a novel Ni imprinting method with high hexagonal pore accuracy and order. The pore diameter after the widening process is about 320 nm. TiO_2 layer is deposited inside the template using atomic layer deposition (ALD) followed by the deposition of 6 nm TiN thin film over the TiO_2 using a direct current (DC) sputtering unit. The prepared nanotubular $TiN/TiO_2/Al_2O_3$ was fully characterized using different analytical tools such as X-ray diffraction (XRD), Energy-dispersive X-ray (EDX) spectroscopy, scanning electron microscopy (SEM), and optical UV-Vis spectroscopy. Exploring the current-voltage relationships under different light intensities, wavelengths, and temperatures was used to investigate the electrode's application before and after Au coating for H_2 production from sewage water splitting without the use of any sacrificing agents. All thermodynamic parameters were determined, as well as quantum efficiency (QE) and incident photon to current conversion efficiency (IPCE). The QE was 0.25% and 0.34% at 400 mW·cm^{-2} for the photoelectrode before and after Au coating, respectively. Also, the activation energy was 27.22 and 18.84 kJ·mol^{-1}, the enthalpy was 24.26 and 15.77 J·mol^{-1}, and the entropy was 238.1 and 211.5 kJ^{-1}·mol^{-1} before and after Au coating, respectively. Because of its high stability and low cost, the prepared photoelectrode may be suitable for industrial applications.

Keywords: Al_2O_3 template; nanomaterials; surface plasmon resonance; photoelectrochemical hydrogen production; sewage water; solar energy conversion

1. Introduction

Renewable energy sources are very important for our life, whereas most of these sources are based on photocatalytic materials that are used in the preparation of solar cells, photodetectors, and photocatalytic electrodes [1–3]. The production of H_2 gas due to water-splitting reaction is a very important energy source for airplanes and factories that used H_2 fuel [4]. The prepared photoelectrode must have high efficiency for water splitting and properties that qualify it for industrial applications, such as low cost, easy preparation, and easy operation [5,6]. The working of the electrode can be carried out under direct sunlight or using another artificial light. Many semiconductor materials were used for the synthesis of the electrode, including oxides, sulfides, and some polymers [7,8]. The properties of the photocatalytic materials improve with increasing the active sites inside the materials, in which the nanowires or nanotube morphology increase the active sites through increasing the surface area of the materials [9,10]. The other way for increasing the efficiency of the electrode is using plasmonic materials for light capture, in which a surface plasmonic resonance is produced from the oscillation of electrons in the conductive bandgap [11].

The most used plasmonic materials are noble metals, such as Au, Ru, Rh, and Pt, but these metals are very expensive [12]. Rabia et al. used Au to enhance the water-splitting reaction for H_2 production under light [13]. Shi et al. used Pt to enhance the activity of CdS materials for water splitting, in which the photoactivity is enhanced very much by using Pt metal [14]. At the same time, many researchers used active metals such as Co, Fe, Ni, and Cu as plasmonic materials. This appears in Cu/ZnO materials, in which the Cu nanomaterials enhance the light capture and efficiency for the light detection in the prepared photodetector [15]. Although these elements are cheap, they are active and easy to form oxides.

With its high noble features and coating protection, metal nitride ceramic can serve as a photo-plasmonic resonance material for light capture, comparable to noble plasmonic metal. These behaviors originate from the chemical stability and high melting point (>2000 K) [16]. Moreover, these metal nitrides are used in designing devices with spectral windows and operating conditions more efficiently in hazardous environmental conditions than noble metals [17]. Some studies were carried out for comparing the effect of TiN and ZrN plasmonic materials on the sensing properties of a plasmonic refractometry sensor with noble metals, finding that the nitride metals were more efficient than the noble metals [16,18–20].

Due to the good properties of the TiN material, such as high hardness, nontoxicity, high thermal conductivity, high corrosion resistance, chemical stability, and high UV-Vis light absorbance, Mohamed et al. used a 9 nm TiN layer to enhance the properties of TiO_2 photoactive material for solar cells [18]. With an increase in TiN thickness to 9 nm, the optical properties, absorption, and bandgap improved, resulting in increased photocurrent. Awad et al. used tri-layered TiO_2/TiN/TiO_2 self-cleaning systems of different TiN thicknesses to optimize their optical properties and facilitate the photodegradation of the organic materials [21]. Also, many researchers have concentrated on the properties of TiN and TiN-based nanostructures for application in many devices, such as fuel cells, supercapacitors, superconductors, and solar cells [22–24].

Photocatalytic properties of TiO_2 materials, especially in structures with a large surface area, such as nanowires and nanorods, are of particular interest [25]. TiO_2 nanotubes tolerate more active sites on their internal and external surfaces that increase their activity in light absorption, in addition to their large surface area-to-volume ratios. TiO_2 also has several desirable characteristics, including nontoxicity, low cost, ease of preparation, and high stability [22]. These properties qualify TiO_2 materials for application in sensors, supercapacitor, H_2 production, solar cell, and light absorbance [26]. Since TiO_2 has a wide bandgap > 3 eV, it can only be used in photocatalytic and light detection devices that operate in the UV range [27].

Many studies on H_2 generation by water splitting have recently been released, but almost all of them use a sacrificing agent, such as NaOH, HCl, $Na_2S_2O_3$, or Na_2SO_3 for water splitting [28–31]. Also, the majority of these studies do not demonstrate long-term H_2 production stability. Furthermore, the morphology of the microsized materials is uncontrolled [30–32]. In this study, a TiN/TiO_2/Al_2O_3 template photoelectrode was created and used to generate H_2 from sewage water splitting without the use of any sacrificing agents. The effect of depositing a thin Au film on the TiN/TiO_2/Al_2O_3 electrode was also investigated. An Al_2O_3 template was prepared with high hexagonal ordering using the Ni imprinting technique. The TiO_2 was deposited using the ALD technique, whereas the thin TiN layer was deposited using the DC sputtering technique. The electrode's application for H_2 production was studied by exploration the current–voltage relationship under various light intensities, wavelengths, and temperatures. The quantum efficiency (QE), incident photon to current conversion efficiency (IPCE), and all thermodynamic parameters were calculated. The prepared photoelectrode can be applicable in the industrial field with high stability and low cost.

2. Experimental Methods

2.1. Al_2O_3 Template Synthesis

The synthesis of the Al_2O_3 template was carried out with a novel method of high controllability in the shape and size of the pores. The aim is to prepare pores with a hexagonal shape with a pore diameter of about 320 nm. For the preparation of the Al_2O_3 template, Al metal (99.99%) was used, in which an electropolishing process was carried out for removing any impurities or corrosions. To determine the position of the pores, the Ni imprinting method was applied at a pressure of ~10 kN/cm^2 for 180 s using an oil pump [24]. Then, a two-step anodization process is carried out using a mixture of H_3PO_4, ethylene glycol, and H_2O with a volume ratio of 1:100:200. The first step was carried out for 15 min, whereas the second step was performed for 120 min at 2 °C. The first step was etched using a mixture of H_2CrO_4 and H_3PO_4 with concentrations of 1.5 wt% and 6 wt%, respectively. As a final step, the nanopores were widened at 60 °C for 20 min.

2.2. Synthesis of TiN/TiO_2 and $Au/TiN/TiO_2$

TiN/TiO_2 nanotubes were prepared inside the Al_2O_3 template through two different steps. The pore of the template was about 320 nm with a length of about 1 μm. First, TiO_2 was synthesized by the atomic layer deposition device (ALD, Picosun SUNALE R150 ALD, Poscosun, Espoo, Finland) at 300 °C for 300 running cycles with a rate of 0.3 nm/s. TiO_2 is prepared from $TiCl_4$ as Ti source and H_2O as O source. After that, TiN thin film (8 nm) was deposited over TiO_2 using DC sputtering device under initial and working pressures of 6.7×10^{-7} and 1.3×10^{-2} mbar, respectively. The sputtering process was carried out from a mixture of N_2 and Ar gases with volumes of 75 and 25 sccm, respectively. The Ti source was a Ti-metal (99.99%). Finally, for synthesis $Au/TiN/TiO_2$, Au nanoparticles are sputter-coated over $TiN/TiO_2/Al_2O_3$ template under vacuum conditions for 3 min. Au deposition was carried out utilizing a fairly basic sputter-coater at pressure 2 torr (low vacuum), current 13 mA, and a distance of 8 cm in front of the Au target. The rate of growth of the Au layer was 5 nm/min.

2.3. Samples Characterization

The prepared template and nanotubes were characterized using different devices. The chemical structure was confirmed using an X-ray diffractometer (XRD, Bruker/Siemens D5000, Aubrey, TX, USA) by Kα radiation of Cu (λ = 1.5405 Å) at 30 mA, and 40 kV. Moreover, the elements inside the materials and nanomorphologies were determined using a scanning electron microscope (SEM, Auriga Zeiss FIB, Zeiss company, Oberkochen, Germany) provided with energy-dispersive X-ray (EDX, Zeiss company, Oberkochen, Germany) unit. The optical properties were characterized using a double beam spectrophotometer (Perkin Elmer Lambda 950, Perkin Elmener company, Waltham, MA 02451, USA).

2.4. Water-Splitting Test

The water-splitting test reaction was carried out under a solar simulator from a two-electrode cell, in which the $TiN/TiO_2/Al_2O_3$ or $Au/TiN/TiO_2/Al_2O_3$ represented the working electrode that worked as a cathode, whereas a graphite electrode with the same dimension was worked as an anode, Figure S1 (Supplementary Data). The chemical composition of the sewerage water is mentioned in Table S1. The pH value was 5 for this wastewater. The effects of light intensity (100 to 400 mW·cm^{-2}), incident wavelength (405 to 636 nm), temperature reaction (30 to 70 °C), and time stability were studied for water splitting for H_2 and O_2 evolutions. The effect of monochromatic light on the water splitting is tested using optical filters of different wavelengths; 405, 470, 490, 508, and 636 nm.

3. Results and Discussion

3.1. SEM and XRD Studies

The morphological analysis of the Al_2O_3 template after pore widening at 60 °C is mentioned in Figure 1a. From this figure, the Al_2O_3 template is prepared with high accuracy and ordering with a hexagonal shape, in which the pore diameter is about 330 nm. Figure 2b displayed the bottom of the membrane after the deposition of TiO_2 by the ALD. The bottoms of the tubes are uniformly coated, whereas the outer diameter of the bottom is about 320 nm. Moreover, the TiN/TiO_2 back surface is shown in Figure 1c, after the deposition of TiN, the diameter is increased to ~330 nm. The cross-section of TiN/TiO_2 is shown in Figure 1d with a length of about 1.0 µm. The bottoms of the tubes become rough with extremely small nanofeatures after TiN deposition. This increases the effective surface area and surface-active sites, allowing TiN to perform its primary function as a plasmonic layer for light absorption. Figure S2 (Supplementary Data) also shows a top-view SEM image of $Au/TiN/TiO_2/Al_2O_3$ with agglomerated Au nanoparticles covering the top-surface and template pores with an average diameter of 285 nm.
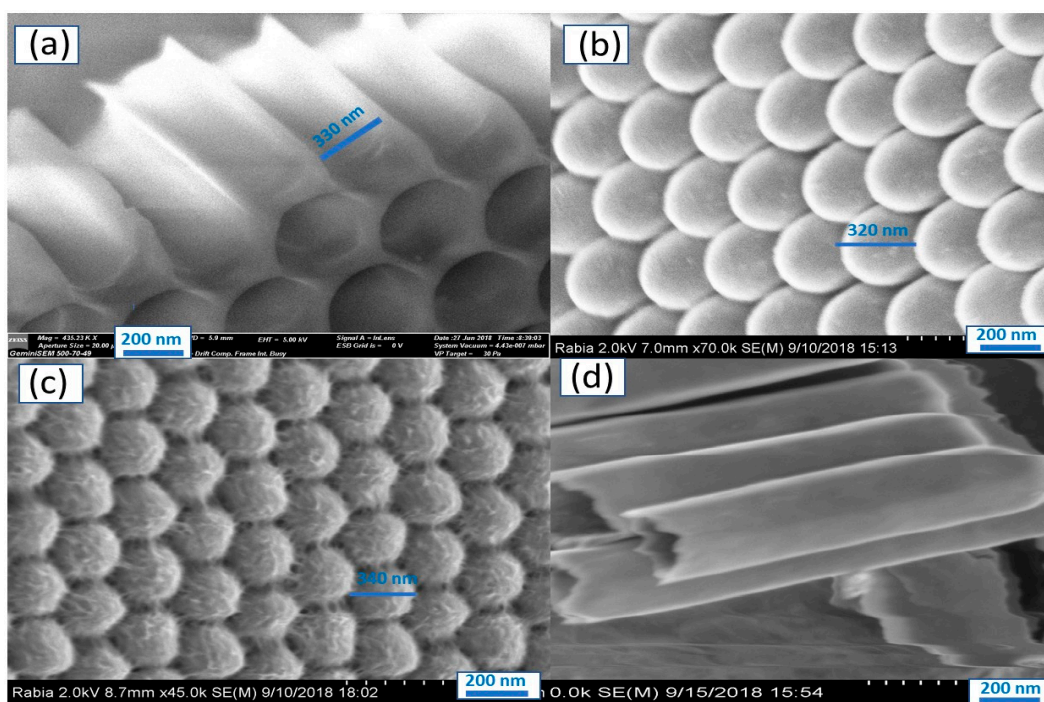

Figure 1. SEM images of (**a**) Al_2O_3 template after pore widening, (**b**) TiO_2, (**c**) TiN/TiO_2, and (**d**) TiN/TiO_2 a cross-section.

The structures and chemical constructions of the prepared materials are confirmed using XRD analyses as shown in Figure 2. The sharp peaks in the XRD of the Al_2O_3 template, Figure 2a, refer to the formation of a crystalline structure with excellent precision and ordering [32]. The Al_2O_3 has three peaks at 44.5°, 65.0°, and 78.1°, which correspond to the growth directions (113), (214), and (119), respectively. In addition, Figure 2a shows the XRD analysis of the synthesized TiN/TiO_2, which shows eight peaks at 25.7°, 38.0°, 48.2°, 54.2°, 55.2°, 62.7°, 69.7°, and 75.4°. These peaks, coupled with the growth directions (101), (103), (200), (105), (211), (213), (118), and (215), indicated the synthesis of anatase TiO_2. The deconvolution of the broadband peak in the XRD pattern of TiN/TiO_2 exhibits the overlapping of two diffraction peaks: (101) peak of anatase-TiO_2 (JCPDS 21-1272) and the adjacent (111) peak of TiN (JCPDS 38-1420). Otherwise, the deposition of ultra-thin TiN film using DC sputtering on TiO_2 does not create any phase change in the XRD pattern [33]. From the XRD of TiN/TiO_2 and the observed peaks for the anatase TiO_2, it can be concluded that the TiO_2 layer was crystalline with preferred growth orientation alongside the (101) direction.
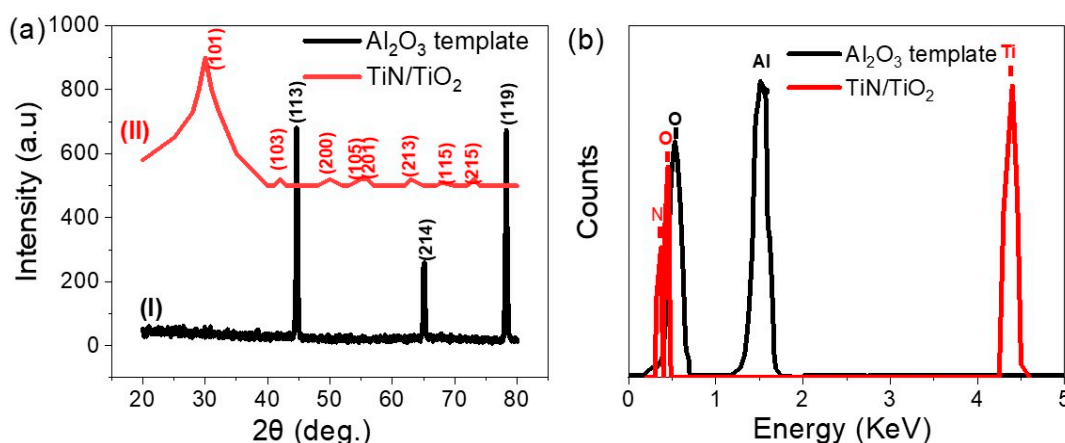
Figure 2. (**a**) XRD and (**b**) EDX of Al_2O_3 template and TiN/TiO_2.

The EDX analyses of the Al_2O_3 template and TiN/TiO_2 are shown in Figure 2. For Al_2O_3, the O and Al elements of the template are detected. For TiN/TiO_2 nanotube; Ti, O, and N signals are detected. In addition, Figure S3 (Supplementary Data) shows the EDX spectrum for $Au/TiN/TiO_2/Al_2O_3$, in which all elements (Ti, O, N, Al, and Au) are well detected. The weight% of the Au is approximately 3%.

3.2. Optical Properties of TiN/TiO$_2$/Al$_2$O$_3$

The optical properties of the prepared template and $TiN/TiO_2/Al_2O_3$ are illustrated in Figure 3. The reflectance spectra of the Al_2O_3 template and $TiN/TiO_2/Al_2O_3$ are displayed in Figure 3a. The reflectance of $TiN/TiO_2/Al_2O_3$ shows stronger interference fringes than that of the Al_2O_3 template alone. In the case of $TiN/TiO_2/Al_2O_3$, constructive and destructive interferences between reflected waves from TiO_2/Al_2O_3, TiN/TiO_2, and air/TiN interfaces are responsible for these strong interference fringes. These interferences are low in the UV and Vis regions and increase in the near IR region. The strength of the interference ripples grows with increasing wavelength; nevertheless, the interference ripple below 600 nm is much stronger. This could be due to the Al_2O_3 blue emission band, which is attributed to mixed emission from F and F^+ centers [34]. After Au nanoparticles deposition, the reflectance values decrease, this indicates the increasing absorbance values. This confirms the main plasmonic role of Au nanoparticles. The reduction of the reflectance in the UV/Vis region indicating that the TiN/TiO_2 materials have strong absorbance in the UV/Vis regions. To confirm that for the TiN/TiO_2, we have measured the absorbance spectra for TiO_2 and TiN/TiO_2 materials, as declared in Figure 3b. Because the anatase bandgap forms between the Ti3d and O2p states, TiO_2 exhibits a good absorbance [34,35]. After TiN deposition, the absorbance is enhanced in which the right edge of the absorption peak is extended in the visible region till 600 nm. This improvement in the absorption behavior came from the main role of the plasmonic TiN material. The bandgap (Eg) values for TiO_2 and TiN/TiO_2 materials, which are 3.1 and 2.2 eV, respectively, demonstrate this improvement in optical properties (Figure 3c). The Eg value was calculated using the Tauc equation, Equation (1), the optical absorption (A), absorption coefficient (α), material thickness (d), light frequency (v), Planck constant (h), and Boltzmann constant (β) [36]:

$$\alpha h\nu = \beta(h\nu - Eg)^{\frac{1}{2}} \tag{1}$$
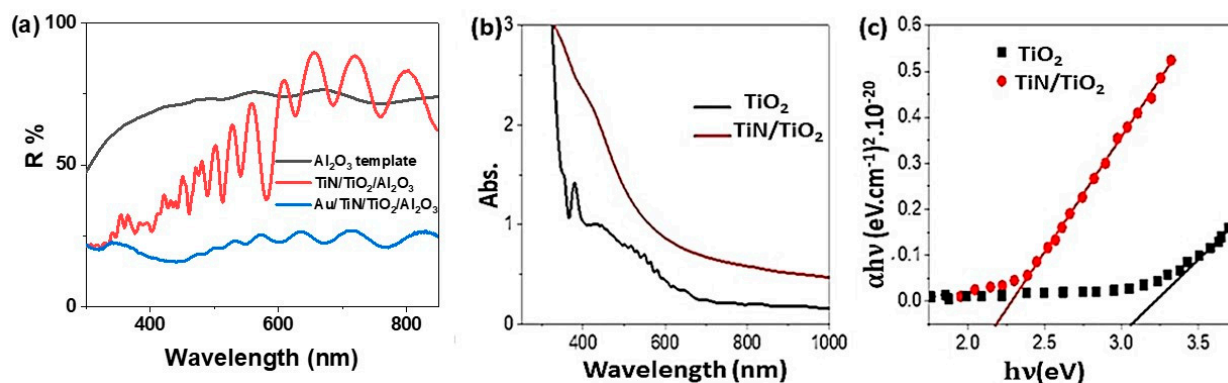
$$\alpha = \left(\frac{2.303}{d}\right)A \tag{2}$$

Figure 3. Optical analyses; (**a**) reflectance (Al_2O_3 template, $TiN/TiO_2/Al_2O_3$, and Au/ $TiN/TiO_2/Al_2O_3$), (**b**) absorption, and (**c**) bandgap calculation for TiO_2 and TiN/TiO_2 nanomaterials.

3.3. The Photoelectrochemical Performance

The electrochemical performances of the prepared electrodes, $TiN/TiO_2/Al_2O_3$ and $Au/TiN/TiO_2/Al_2O_3$, for the H_2 generation are measured under lighting from a metal-halide Lamp (Newport, 66926-500HX-R07). The measurements were carried out using the Keithley measurement source unit (model:2400), whereas the J_{ph} value represents the H_2 generation rate from the waste H_2O (sewage water). The relation between current density and voltage for the $TiN/TiO_2/Al_2O_3$ electrode with and without Au coating is revealed in Figure 4A,B shows how the $TiN/TiO_2/Al_2O_3$ electrode functioned as a photocathode for the generation of H_2. Under light irradiation, the resultant current density is -0.0924 mA·cm^{-2} @ -1 V, as shown in Figure 4A. Figure 4B shows that this electrode's performance for O_2 production is poor, with a current density of just 0.0295 mA·cm^{-2} @ 1 V and an onset value of -0.0202 mA·cm^{-2} @ 0 V. While the Au-coated electrode in Figure 4C,D is utilized to split water and produce O_2, the opposite electrode produces H_2 (graphite-electrode). With an onset value of 0.0143 mA·cm^{-2} @ 0 V, the current density was -0.127 mA·cm^{-2} @ -1 V and 0.140 mA·cm^{-2} @ 1 V. As a result, the $Au/TiN/TiO_2/Al_2O_3$ electrode performed better as a photoanode for O_2 generation, as shown in Figure 4C,D). The generated current density has increased significantly, Figure 4D, reaching 0.140 mA·cm^{-2}. This enhancement in the produced current density is due to the plasmonic resonance of Au nanoparticles and their role in the enhancement of near IR absorbance and hot-electron allocation [36–38]. In addition to that, the existence of Au nanoparticles on the electrode surface causes light multiple reflections and mean photon path elongation alongside the catalytic electrode. Additionally, because the Fermi level (EF) of Au NPs is lower than that of TiO_2, light excites electrons at the Fermi level of plasmonic Au NPs and raises them to the localized surface plasmon energy level. This permits surface plasmon-generated hot electrons to be transported to the conduction band (CB) of TiO_2, resulting in enhanced charge carriers and photocurrent. Also, Au nanoparticles facilitate the excitation of the electron to overcome the Schottky barrier and reach the conducting band of TiO_2/TiN. Also, plasmonic Au NPs were able to widen the light absorption band to the visible region. As a result, the incorporation of Au NPs reduces electron-hole recombination and improves light absorption, resulting in improved photocatalytic activity.
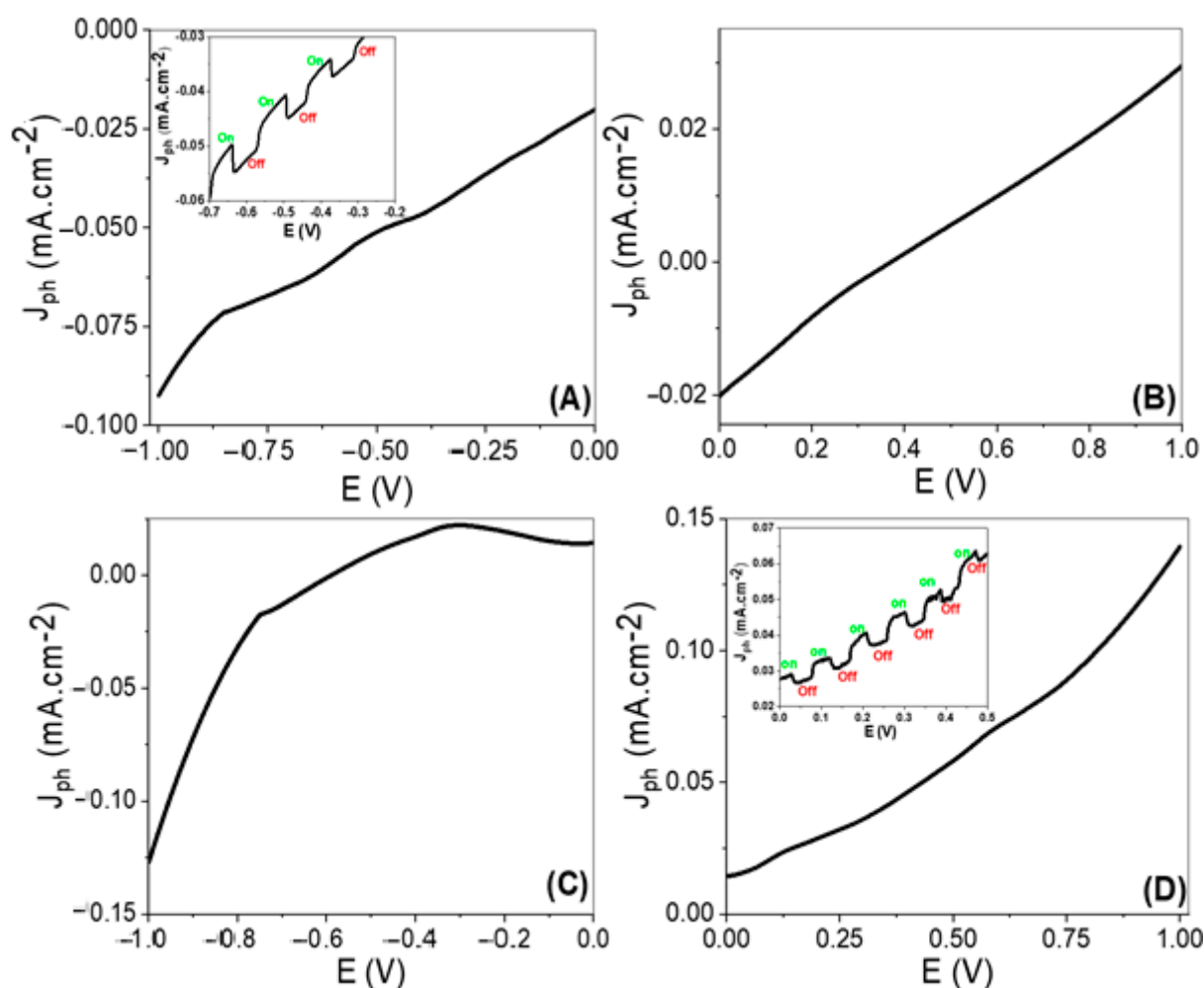
Figure 4. The current density (J_{ph}) –voltage curves for (**A,B**) TiN/TiO$_2$/Al$_2$O$_3$ and (**C,D**) Au/TiN/TiO$_2$/Al$_2$O$_3$ electrodes.

The chopped current density versus the applied voltage is illustrated in Figure 4A,B. From Figure 4A, there is a change in the current density value with on and off light. This indicates the high activity of the TiN/TiO$_2$/Al$_2$O$_3$ electrode for water splitting and the PEC H$_2$ generation process. Also, Au/TiN/TiO$_2$/Al$_2$O$_3$ electrode chopped current density is appeared clearly with on and off light.

The effect of light intensity on the prepared TiN/TiO$_2$/Al$_2$O$_3$ electrode is referred to in Figure 5a. The produced J_{ph} increases with increasing the light intensity from 100 to 400 mW. This is clearly appearing in the inset figure, whereas the J_{ph} is increased from 0.076 to 0.096 mA·cm^{-2}, respectively. As the light intensity increased, the J_{ph} increases due to the increasing electron-hole pair generation [39,40]. With increasing the light intensity, many photons per second reach the active sites of the photocatalytic material to generate free electrons at the active sites of the TiO$_2$/TiN catalyst. The produced current is directly proportional to the absorbed light intensity [41]. The J_{ph} represents the current density produced in the cell due to the water splitting, in which J_{ph} can represent the rate of H$_2$ or O$_2$ evolution [41,42].
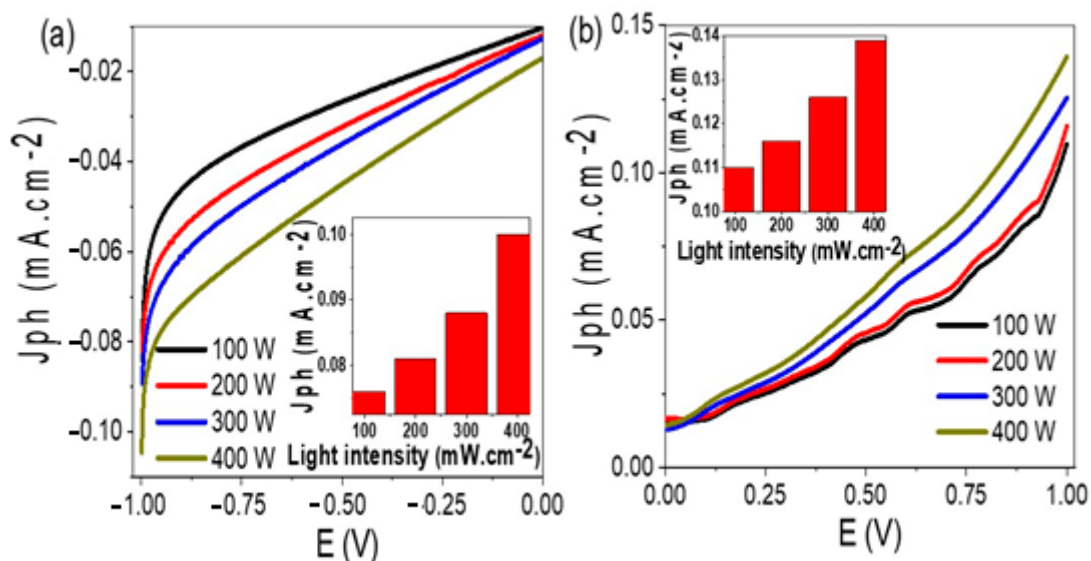
Figure 5. The effect of incident light intensity on the current density-voltage characteristics for (**a**) TiN/TiO$_2$/Al$_2$O$_3$ and (**b**) Au/TiN/TiO$_2$/Al$_2$O$_3$ electrodes.

On the other hand, after coating the electrode with Au nanoparticles, the produced J$_{ph}$ value increases, Figure 5b, in which the J$_{ph}$ value changed from 0.10 to 0.139 mA·cm^{-2} with increasing the light intensity from 100 to 400 mW·cm^{-2}, respectively.

The quantum efficiency (QE) is the relation between the incident light photons (intensity) and produced electrons (current intensity), in which QE can be calculated using Equation (4) [43], whereas the photon flux (number of photons per second), N, can be calculated using Equation (3).

$$N = P \cdot \lambda / hc \tag{3}$$

$$QE = J_{ph}C/N = J_{ph} \cdot h \cdot C \cdot c / P \cdot \lambda \tag{4}$$

Here, h is the Plank's constant (6.626 $\times$ 10^{-34} J/s), c is the light speed in space (3 $\times$ 10^8 m/s), P is the light intensity (W·m^{-2}), and λ is the light wavelength (405 $\times$ 10^{-9} m).

The value of N is directly proportional with the light intensity as shown in Figure S4, in which N is changed from 2 $\times$ 10^{21} to 8 $\times$ 10^{21} photon/sec as the light intensity changed from 100 to 400 mW·cm^{-2}. On the other hand, the QE and light intensity are almost inversely proportional to each other. The QE for TiN/TiO$_2$/Al$_2$O$_3$ is changed from 0.25% to 0.08% with changing the light intensity from 100 to 400 mW·cm^{-2}, Figure 6a. Also, the QE for Au/TiN/TiO$_2$/Al$_2$O$_3$ is changed from 0.34% to 0.1% with changing the light intensity from 100 to 400 mW·cm^{-2}, Figure 6b. From Figure 6a,b, it can be seen that there is more enhancement in the QE after Au coating. This is related to the role of Au in enhancing the catalytic properties of the catalyst and improving light absorption. The contact of the electrode with the sewage water causes increasing of the local charges around Au nanoparticles. These local charges enhance the photocatalytic activity of the electrode and increase the water-splitting reaction rate. Furthermore, due to the strong corrosion resistance of Au under most environmental conditions, the layer of the Au nanoparticles on the surface protects the underlying layers and increases the photoelectrode stability [44].
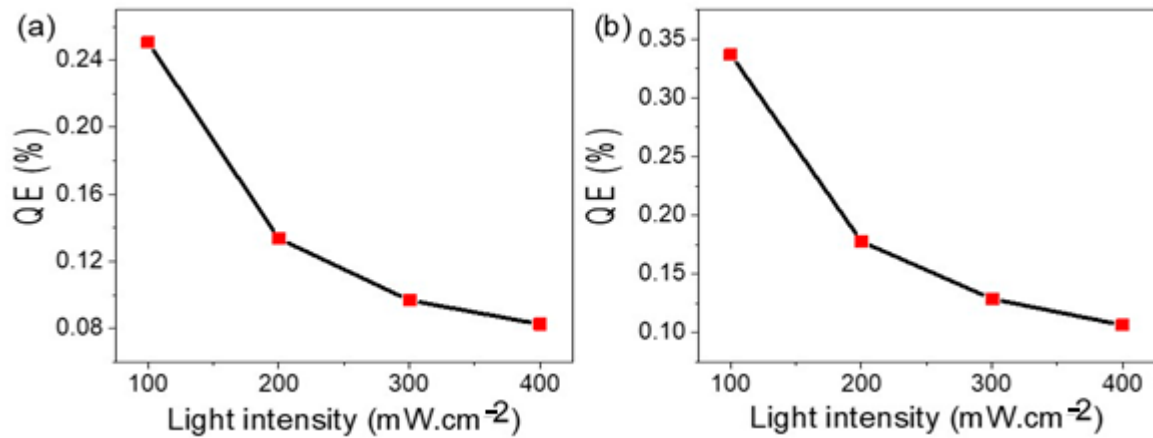
Figure 6. The relation between quantum efficiency and light intensity for (**a**) $TiN/TiO_2/Al_2O_3$ and (**b**) $Au/TiN/TiO_2/Al_2O_3$ electrodes at 405 nm.

The effect of monochromatic light on the produced J_{ph} for $TiN/TiO_2/Al_2O_3$ and $Au/TiN/TiO_2/Al_2O_3$ electrodes is shown in Figure 7a,b, respectively. From Figure 7a, it can be seen that the J_{ph} value is changed under the monochromatic light effect, in which 405 nm light has the optimum J_{ph} value ($-0.092 \text{ mA}\cdot\text{cm}^{-2}$). This behavior is matched well with the absorption light spectrophotometry for this electrode.

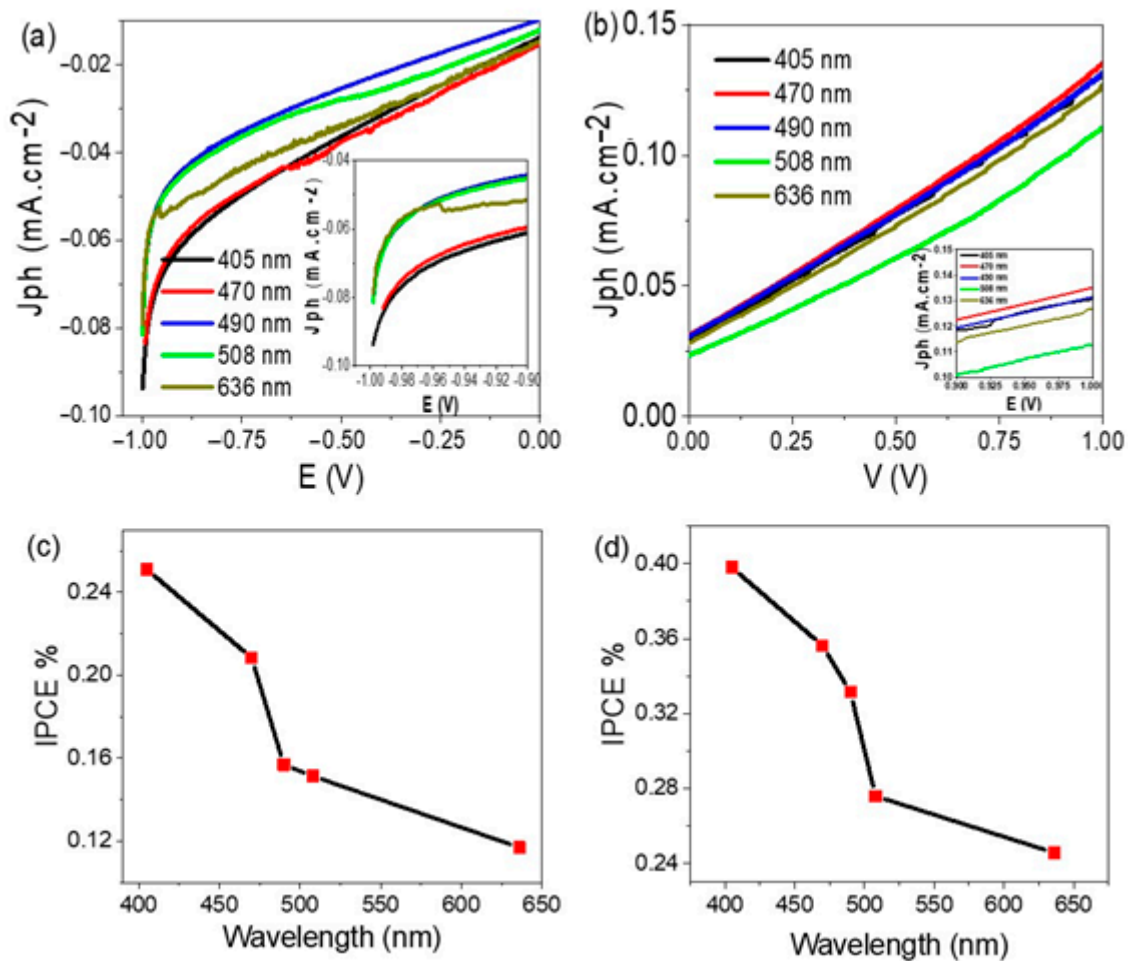

Figure 7. (**a**,**b**) The current density-voltage characteristics under the effect of monochromatic light, and (**c**,**d**) the IPCE for $TiN/TiO_2/Al_2O_3$ and $Au/TiN/TiO_2/Al_2O_3$ electrodes, respectively.

On the other hand, the effect of monochromatic light on $Au/TiN/TiO_2/Al_2O_3$ electrode is shown in Figure 7b; the J_{ph} value is changed with the wavelength of the incident light. The irradiance power versus the optical wavelength (irradiance spectrum) of the 66,142–500W Hg (Xe) lamp is presented in Figure S5. The wavelength 470 nm has the optimum J_{ph} value (0.137 mA·cm^{-2}), then wavelength 405 nm has a value of 0.131 mA·cm^{-2}. The incident photon to current conversion efficiency (IPCE) describes the photocurrent produced due to photon flux. It can be calculated from the wavelength values [45]. The IPCE is calculated from Equation (5).

$$IPCE = \frac{J_{ph}\left(mA\cdot cm^{-2}\right)\cdot 1240\ (V\cdot nm)}{P(mW\cdot cm^{-2})\cdot \lambda(nm)} \tag{5}$$

The IPCE is calculated for $Al/Al_2O_3/TiO_2/TiN$ as shown in Figure 7c at a light intensity of 100 mW·cm^{-2}. From Figure 7c, it can be seen that the electrode has the optimum IPCE of 0.25% at 405 nm. This value is decreased by increasing the wavelength to 636 nm. Moreover, after coating the electrode with Au nanoparticles, the IPCE increases to 0.39% at 405 nm. Then, the value decreases with increasing the wavelength from 405 to 636 nm. The IPCE value results from the effect of the photocatalytic property of the electrode for sewage water splitting without adding an external electrolyte. Therefore, the electrode works for converting the sewage water to H_2 and O_2 with higher efficiency than that reported by other previous studies [28,46–50].

3.4. Effect of Temperature and Thermodynamic Parameters

The temperature effect on the $TiN/TiO_2/Al_2O_3$ electrode for H_2 production due to water splitting is presented in Figure 8a, in which the J_{ph} increases from -0.1 to -0.28 mA·cm^{-2} with increasing the temperature from 30 to 60 °C. On the other hand, the temperature has the same effect on the electrode after Au coating, $Au/TiN/TiO_2/Al_2O_3$, as shown in Figure 8b. in which the J_{ph} value increases from 0.13 to 0.33 mA·cm^{-2} with increasing the temperature from 30 to 70 °C, respectively. The general increases in J_{ph} values represent the reaction rate, which reflects the H_2 and O_2 production rate [51,52].

From the Arrhenius equation, Equation (6), the activation energy (Ea) can be calculated depending on the particles collision and the rate of water splitting, in which k, R, and A are the rate, universal gas, and Arrhenius constants, respectively, and T is the absolute temperature [53]. From the Ea value, the degree of reaction occurrence is determined [54–56].

$$k = Ae^{-Ea/RT} \tag{6}$$

From Figure 8c,d, it can be seen that the slope values of the relation $\ln J_{ph}$ and $1/T$ give Ea values. The Ea values are 27.22 and 18.84 kJ·mol^{-1} for electrodes $Al/Al_2O_3/TiO_2/TiN$ and $Al/Al_2O_3/TiO_2/TiN/Au$, respectively. The Ea values for both electrodes are low when compared to earlier published data for other photocatalysts [54–58]. So, the prepared electrodes are efficient for H_2 and O_2 evolution due to the water-splitting reaction [57]. Therefore, the Au coating over the $Al/Al_2O_3/TiO_2/TiN$ electrode has a significant role in decreasing the Ea energy and increasing the probability of water-splitting occurrence. This is related to the plasmonic effect of Au nanoparticles and light capture phenomena [58]. In the same manner, the enthalpy (ΔH^*) and entropy (ΔS^*) can be estimated from the Eyring equation, Equation (7), using the Boltzmann constant (kB) and the Planck constant (h) [59,60].

$$k = T\cdot\frac{kB}{h}\cdot e^{\Delta S/R}\cdot e^{-\Delta H/RT} \tag{7}$$

For calculating the ΔH^* and ΔS^* values, the slope, and intercept from Figure 8e,f are used. The values of ΔH^* for $TiN/TiO_2/Al_2O_3$ and $Au/TiN/TiO_2/Al_2O_3$ electrodes are 24.26 and 15.77 J·mol^{-1}, respectively, while ΔS^* values are 238.1 and 211.5 kJ^{-1}·mol^{-1}.
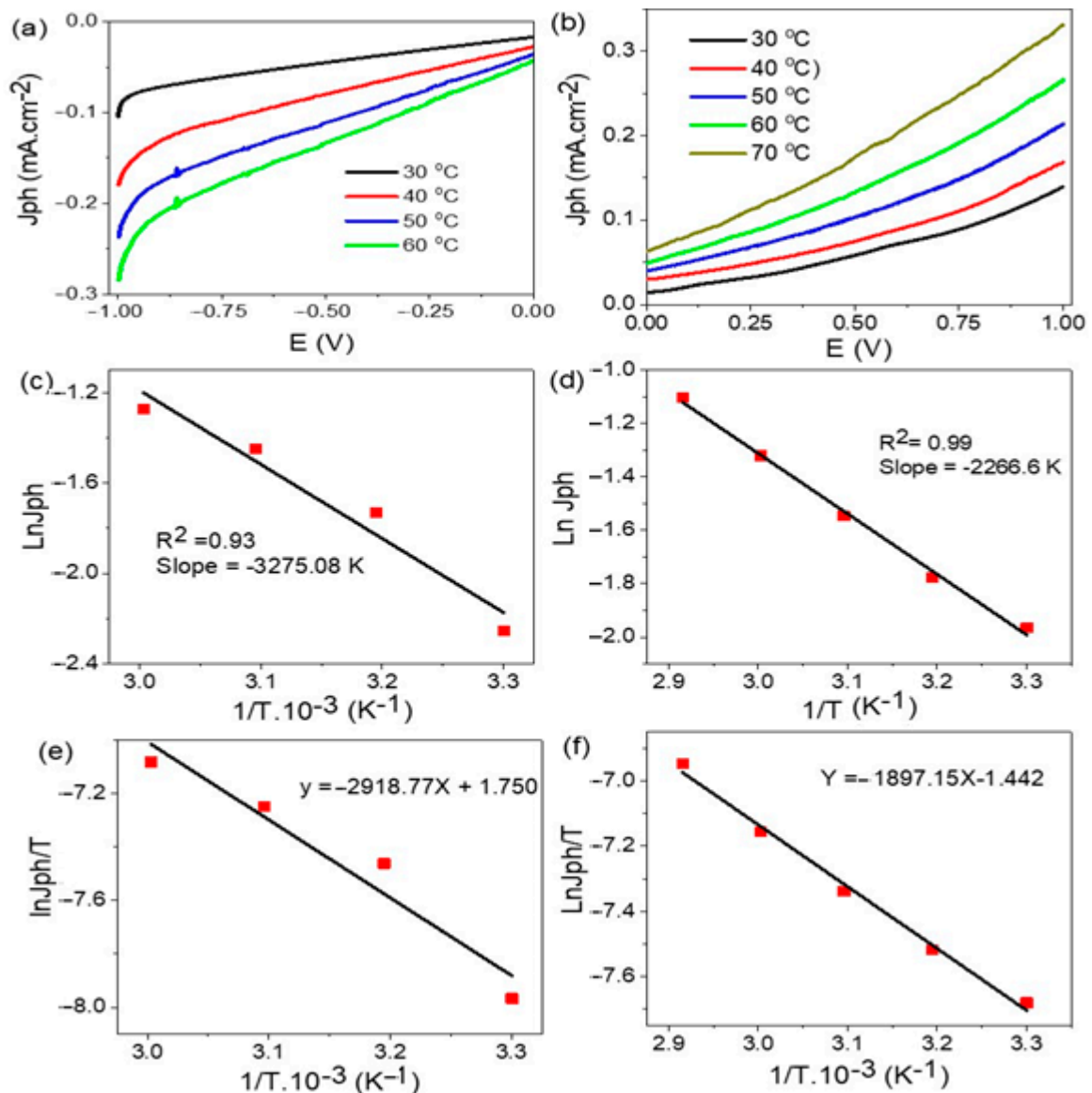
Figure 8. The temperature effect, activation energy, and heat of reaction on (**a**,**c**,**e**) $TiN/TiO_2/Al_2O_3$ and (**b**,**d**,**f**) $Au/TiN/TiO_2/Al_2O_3$ electrodes, respectively.

3.5. Stability of the Photoelectrode

The stability of the prepared $TiN/TiO_2/Al_2O_3$ and $Au/TiN/TiO_2/Al_2O_3$ photoelectrodes was studied as illustrated in Figure 9a,b. The stability represents the relation between time and the produced J_{ph} value by applying a potential of -0.9 and 0.9 V on the two electrodes before and after Au coating, respectively. From Figure 9a, the electrode without Au is stable with time (1000 s) at about -0.06 mA·cm^{-2}. After Au coating, the J_{ph} value becomes stable at about 0.07 mA·cm^{-2}, Figure 9b. These values indicate the TiN and Au coating materials have high stability and anticorrosion properties that maintain the produced J_{ph} at the same values with time [13,61]. This means that every small change in the produced J_{ph} value refers to a small corrosion reaction due to the acidity of the sewage water.
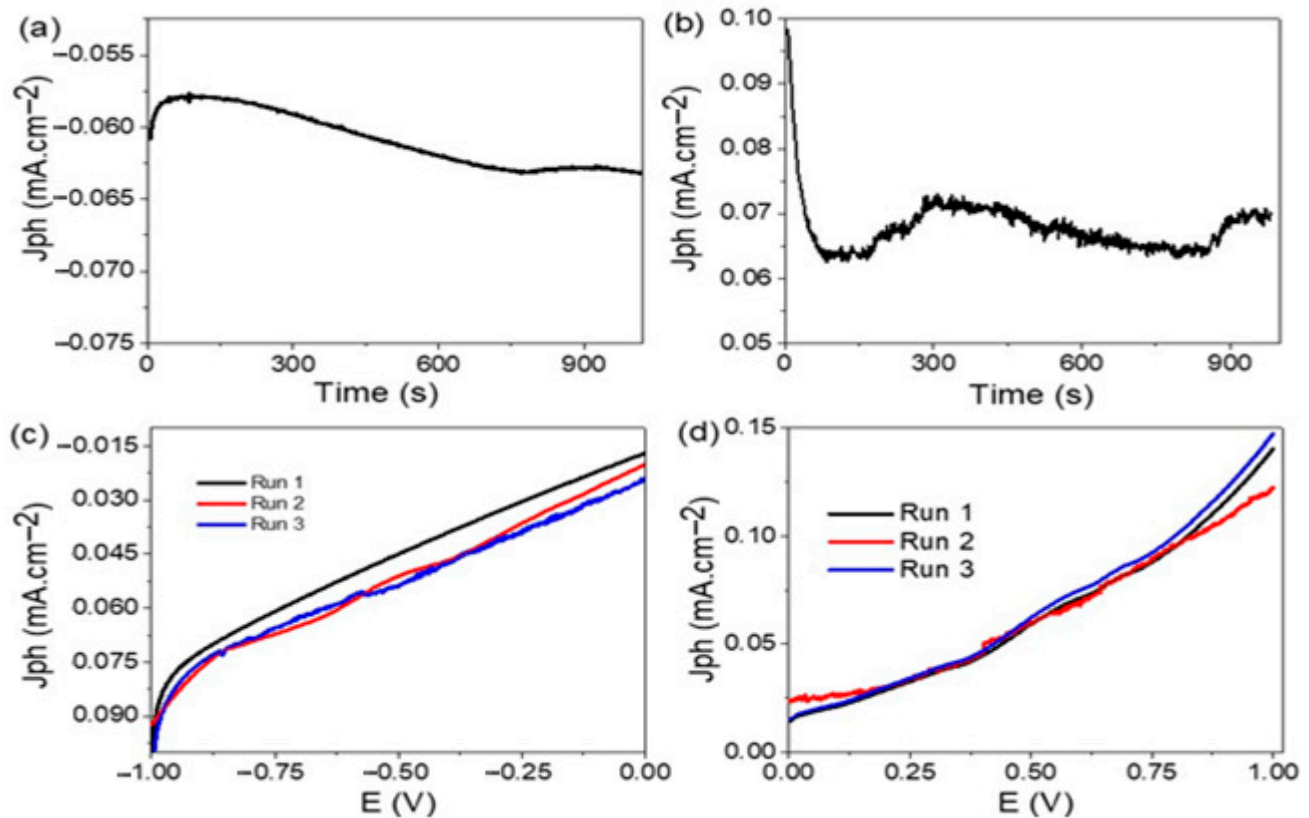
Figure 9. The stability and reproducibility of (**a**,**c**) TiN/TiO$_2$/Al$_2$O$_3$ and (**b**,**d**) Au/TiN/TiO$_2$/Al$_2$O$_3$ electrodes.

As illustrated in Figure S6, the number of H$_2$ and O$_2$ moles was determined using Equation (8) [62,63], where F is the Faraday constant and dt is the time change.

$$H_2 \text{ mole} = \int_0^t J_{ph} \cdot dt / F \tag{8}$$

According to the graph, both gases increase with time, corresponding to 7369.6 and 7915.0 mol h^{-1} cm^{-2} for H$_2$ and O$_2$, respectively.

The reproducibility of the TiN/TiO$_2$/Al$_2$O$_3$ and Au/TiN/TiO$_2$/Al$_2$O$_3$ photoelectrodes is demonstrated in Figure 9c,d, respectively, by repeating the relation between current density and voltage three times at 30 °C under the simulated sunlight. The standard deviation (SD) values for the two photoelectrodes are 0.3% and 1.29%, respectively.

For comparison, the performance indicators, J$_{ph}$ and IPCE, of the prepared electrodes are displayed in Table 1 relative to some previously reported electrodes for the water-splitting reaction to evaluate O$_2$ and H$_2$ [28,46,47,50,63,64]. In addition to the low cost and high controllability of the prepared nanomaterials, our prepared photoelectrode has relatively high IPCE and J$_{ph}$ values comparative to the previously reported photoelectrodes in Table 1.

Table 1. Comparison of the IPCE and J_{ph} values of the prepared photoelectrodes with previous work.

Photoelectrode	Electrolyte	J_{ph}	IPCE % (405 nm)	Ref.
$BiFeO_3$	H_2SO_4	0.1 mA·cm^{-2}	0.21	[28]
PrFeO	H_2SO_4	-130 μA·cm^{-2}	-	[46]
Au/Pb(Zr, Ti)O_3	H_2SO_4	0.06 mA·cm^{-2}	0.2	[47]
Poly(3-aminobenzoic acid) frame	H_2SO_4	0.08 mA·cm^{-2}	-	[50]
TiN-TiO$_2$	H_2SO_4	3.0 nA·cm^{-2}	0.03	[64]
TiN/TiO$_2$/Al$_2O_3$	Sewage water	0.09 mA·cm^{-2}	0.25	Present work
Au/TiN/TiO$_2$/Al$_2O_3$	Sewage water	0.14 mA·cm^{-2}	0.39	

3.6. Mechanism of Electron Transition

There are two types of photocatalytic mechanisms for TiN/TiO$_2$ and Au/TiN/TiO$_2$: (1) photo-induced hot-electron transfer to an adjacent reactant, namely interfacial charge transfer, and (2) localized surface plasmon resonance (LSPR)-based electron-hole separation, namely radiative energy transfer, which requires the plasmonic band to be connected with the TiO2 band gap. Optical and electrochemical experiments were used to investigate the two types (Figures 3a, 4 and 10). Furthermore, the number of H$_2$ and O$_2$ moles has been computed (Figure S6).
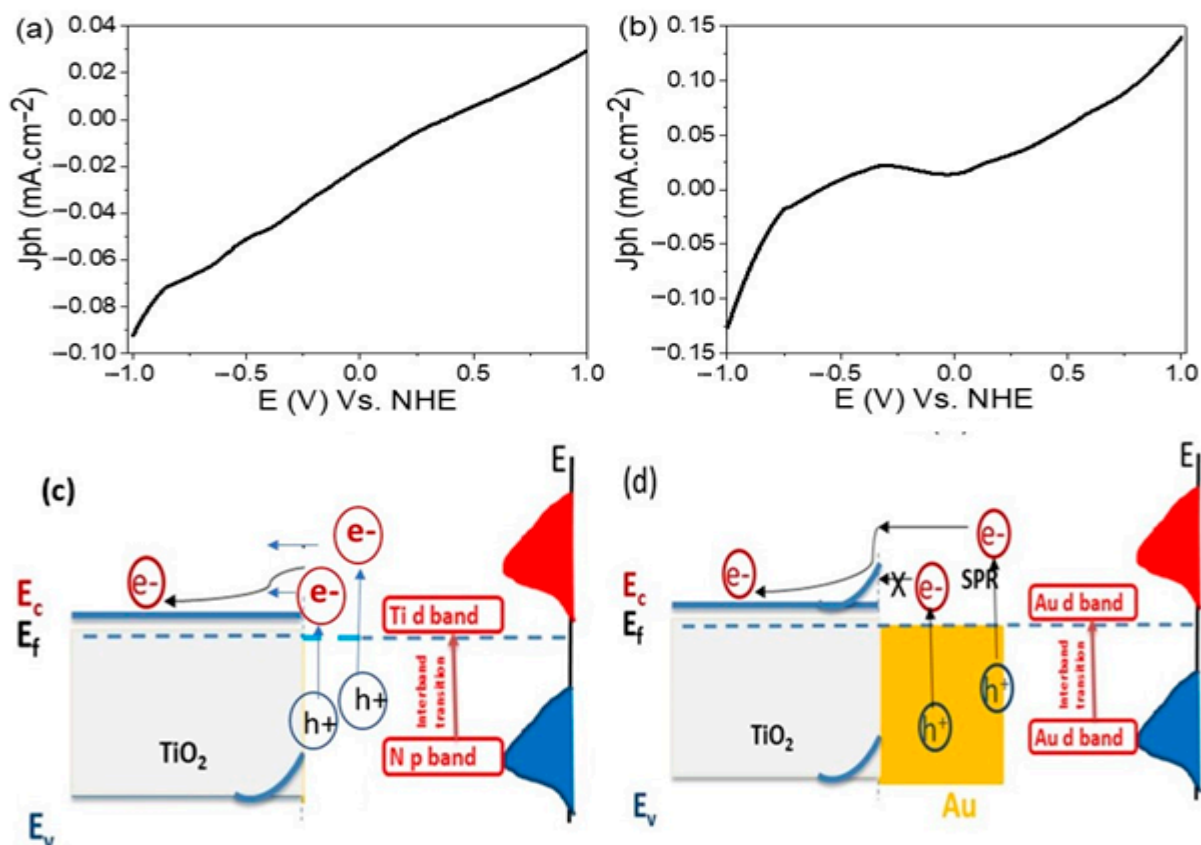

Figure 10. The current density-voltage characteristics and mechanism of electron transition for (**a**,**c**) TiN/TiO$_2$ and (**b**,**d**) Au/Tins/TiO$_2$.

To boost the photocatalytic optical trapping capability and photoelectric conversion rate, this approach uses LSPR to produce enhanced local electromagnetic fields around the TiO$_2$ photocatalyst. The aim is to create finely regulated TiN or Au nanostructures with suitable LSPR coupling to the incident light [65,66]. Plasmonic improves light absorption and broadens TiO$_2$ absorption in this case [67]. The increased electromagnetic field formed

by the coupling between incident light and plasmonic materials transmits radiative energy from the TiN or/and Au plasmonic materials to the semiconducting TiO_2. The UV-visible spectra of the TiN/TiO_2 reveal absorption bands between 350 and 600 nm representing the surface plasmon resonance energy, as shown in Figure 3b. The intense absorption is associated with the considerable enhancement in the electromagnetic field in the vicinity of the TiN nanomaterials. As a result, it is realistic to expect TiN nanoparticles to enable a long-lived LSPR process with high-optical cross-sections and tunable throughout a broad energy range, including deep into the UV and Vis [68].

When plasmonic materials' LSPR modes are coupled with TiO_2, the resultant broadens, resulting in increased coupling efficiency with incident light. By enhancing light absorption, promoting electron-hole creation, and heating the surrounding area, this enhanced field can be used to improve photocatalytic performance [69]. When a TiO_2 photocatalytic layer is applied to the plasmonic structure, the increased field is confined to the interior of the TiO_2 layer, and the plasmon-induced electron-hole pairs diffuse to the photocatalytic surface, contributing to the photocatalytic process. The plasmonic response in the near UV spectrum rises with size t, it can be concluded.

The increased electromagnetic field formed by the interaction of incident light and plasmonic materials transfers radiative energy from the plasmonic materials to the semiconducting TiO_2 [70]. The radiative energy boosts the photocatalysis efficiency when the LSPR energy is coupled with the TiO_2 bandgap, otherwise, the energy is more likely to decay nonradiatively through electron–phonon interactions and no significant enhancement in the photocatalytic activity can be observed [71].

At the TiO_2/plasmonic interface, a significant redistribution of charge occurs depending on the plasmonic work function and the semiconductor electron affinity. In the n-type TiN/TiO_2 and Au nanomaterials, the charge redistribution forms the Schottky barrier which builds up an internal electric field inside the photocatalyst. The electric field facilitates the transfer of the photoexcited electrons and suppressing electron/ hole recombination and improving the quantum efficiency of photocatalysis.

The TiN nanostructures possess a localized plasmonic resonance in the visible and near IR region, similar to the Au nanostructures [72,73]. The difference between the behavior of TiN and Au nanostructure is that TiN produces Ohmic junction whereas Au forms Schottky junction with TiO_2 material [64]. Moreover, TiN is a low-cost material with corrosion resistance and mechanical strength properties. The enhancement in the photocatalytic properties with incorporation in the TiO_2 materials is related to the conversion of energy into electrons below the bandgap of TiO_2 but limits the potential barrier. TiN has a work function QM of about 4 eV in a vacuum, which matches with the TiO_2 electron affinity, and this forms an energetic alignment for the hot electrons [74].

From Figure 10a,c, it can be seen that the fabricated TiN/TiO_2 photoelectrode has an Ohmic junction, which facilitates the electron transition to TiO_2 without barriers. These electrons contribute to the water-splitting reaction and the negative potential is expected to facilitate the H_2 production. On the other hand, incorporating Au nanoparticles boosts photocurrent density while simultaneously forming a Schottky circuit, as seen in Figure 10b,d [74]. As a result, not all electrons absorbed by Au nanoparticles can travel to TiN and TiO_2 materials for water splitting (cold electrons), while hot electrons can only pass through the barrier for the water-splitting reaction. So, the addition of Au nanomaterial increases the potential to be a positive value.

4. Conclusions

This work is very interesting for H_2 production from sewage water using $TiN/TiO_2/Al_2O_3$ nanotube material. The Al_2O_3 template has been prepared with high accuracy and ordering with hexagonal pores using the Ni imprinting method. TiN/TiO_2 is deposited inside the pore using ALD and DC sputter-coating method, respectively. Characteristic analyses of the structural, morphological, and optical properties were carried out for the prepared template and nanotube materials. The application of the $TiN/TiO_2/Al_2O_3$ materials as

photocathode carried out with and without Au nanoparticles coating, in which the Au materials facilitate the sewage water-splitting reaction. The effect of different parameters was studied for water-splitting reaction, such as light intensity, light wavelength, and temperature. The values of QE and IPCE were calculated with a value of 0.34 and 0.39% at 400 nm. Moreover, all thermodynamic parameters are calculated for the photocathode for H_2 production, wherein Ea, ΔH^*, and ΔS^* values were 18.84 kJ·mol^{-1}, 15.77 J·mol^{-1}, and 211.5 kJ^{-1}·mol^{-1} for $Au/TiN/TiO_2/Al_2O_3$ photoelectrode.

Supplementary Materials: The following are available online at https://www.mdpi.com/article/10.3390/nano11102617/s1, Figure S1: Testing the prepared materials as a photocathodem, Figure S2. SEM image of $Au/TiN/TiO_2/Al_2O_3$, Figure S3. EDX of $Au/TiN/TiO_2/Al_2O_3$, Figure S4. The relation between the number of photons per second and the incident light intensity, Figure S5. Irradiance spectrum of 66142 500 W Hg(Xe) lamp, Figure S6. The number of moles evolved (a) H_2 and (b) O_2 gas, Table S1. The chemical composition of the sewerage water used for the H_2 generation.

Author Contributions: Conceptualization, M.R. and M.S.; methodology, M.R., M.S. and H.M.; validation, M.R. and M.S.; formal analysis, M.R. and M.S.; investigation, A.A., M.R. and M.S.; resources, A.A., M.R. and M.S.; data curation, A.A., M.R. and M.S.; writing—original draft preparation, M.R. and M.S.; writing—review and editing, A.A., M.R., H.M. and M.S.; visualization, A.A., M.R., H.M. and M.S.; project administration, A.A., M.R. and M.S.; funding acquisition, A.A., M.R. and M.S. All authors have read and agreed to the published version of the manuscript.

Institutional Review Board Statement: Not applicable.

Informed Consent Statement: Not applicable.

Data Availability Statement: Not applicable.

Conflicts of Interest: The authors declare no conflict of interest.

References

1. Kunwar, S.; Pandit, S.; Jeong, J.H.; Lee, J. Improved Photoresponse of UV Photodetectors by the Incorporation of Plasmonic Nanoparticles on GaN Through the Resonant Coupling of Localized Surface Plasmon Resonance. *Nano-Micro Lett.* **2020**, *12*, 1–16. [CrossRef] [PubMed]
2. Chen, H.; Liu, K.; Hu, L.; Al-Ghamdi, A.A.; Fang, X. New concept ultraviolet photodetectors. *Mater. Today* **2015**, *18*, 493–502. [CrossRef]
3. Tan, M.; Hu, C.; Lan, Y.; Khan, J.; Deng, H.; Yang, X.; Wang, P.; Yu, X.; Lai, J.; Song, H. 2D Lead Dihalides for High-Performance Ultraviolet Photodetectors and their Detection Mechanism Investigation. *Small* **2017**, *13*, 1702024. [CrossRef] [PubMed]
4. Wang, Y.; Qian, Y.; Kong, X. Photon Counting Based on Solar-Blind Ultraviolet Intensified Complementary Metal-Oxide-Semiconductor (ICMOS) for Corona Detection. *IEEE Photonics J.* **2018**, *10*. [CrossRef]
5. Shaban, M.; Rabia, M.; El-Sayed, A.M.A.; Ahmed, A.; Sayed, S. Photocatalytic properties of PbS/graphene oxide/polyaniline electrode for hydrogen generation. *Sci. Rep.* **2017**, *7*, 1–13. [CrossRef] [PubMed]
6. Shaban, M.; Benghanem, M.; Almohammedi, A.; Rabia, M. Optimization of the Active Layer P3HT:PCBM for Organic Solar Cell. *Coatings* **2021**, *11*, 863. [CrossRef]
7. Kang, Z.; Cheng, Y.; Zheng, Z.; Cheng, F.; Chen, Z.; Li, L.; Tan, X.; Xiong, L.; Zhai, T.; Gao, Y. MoS2-Based Photodetectors Powered by Asymmetric Contact Structure with Large Work Function Difference. *Nano-Micro Lett.* **2019**, *11*, 1–12. [CrossRef] [PubMed]
8. Lee, J.H.; Lee, W.W.; Yang, D.W.; Chang, W.J.; Kwon, S.S.; Park, W.I. Anomalous Photovoltaic Response of Graphene-on-GaN Schottky Photodiodes. *ACS Appl. Mater. Interfaces* **2018**, *10*, 14170–14174. [CrossRef] [PubMed]
9. Zhang, X.; Li, J.; Yang, W.; Leng, B.; Niu, P.; Jiang, X.; Liu, B. High-Performance Flexible Ultraviolet Photodetectors Based on AZO/ZnO/PVK/PEDOT:PSS Heterostructures Integrated on Human Hair. *ACS Appl. Mater. Interfaces* **2019**, *11*, 24459–24467. [CrossRef]
10. Kim, J.; Lee, H.C.; Kim, K.H.; Hwang, M.S.; Park, J.S.; Lee, J.M.; So, J.P.; Choi, J.H.; Kwon, S.H.; Barrelet, C.J.; et al. Photon-triggered nanowire transistors. *Nat. Nanotechnol.* **2017**, *12*, 963–968. [CrossRef]

11. Zhang, X.; Liu, Q.; Liu, B.; Yang, W.; Li, J.; Niu, P.; Jiang, X. Giant UV photoresponse of a GaN nanowire photodetector through effective Pt nanoparticle coupling. *J. Mater. Chem. C* **2017**, *5*, 4319–4326. [CrossRef]

12. Rabia, M.; Mohamed, H.S.H.; Shaban, M.; Taha, S. Preparation of polyaniline/PbS core-shell nano/microcomposite and its application for photocatalytic H$_2$ electrogeneration from H$_2$O. *Sci. Rep.* **2018**, *8*, 1107. [CrossRef]

13. Rabia, M.; Shaban, M.; Adel, A.; Abdel-Khaliek, A.A. Effect of plasmonic au nanoparticles on the photoactivity of polyaniline/indium tin oxide electrodes for water splitting. *Environ. Prog. Sustain. Energy* **2019**, *38*, 13171. [CrossRef]

14. Shi, X.F.; Xia, X.Y.; Cui, G.W.; Deng, N.; Zhao, Y.Q.; Zhuo, L.H.; Tang, B. Multiple exciton generation application of PbS quantum dots in ZnO@PbS/graphene oxide for enhanced photocatalytic activity. *Appl. Catal. B Environ.* **2015**, *163*, 123–128. [CrossRef]

15. Li, M.; Yu, M.; Su, D.; Zhang, J.; Jiang, S.; Wu, J.; Wang, Q.; Liu, S. Ultrahigh Responsivity UV Photodetector Based on Cu Nanostructure/ZnO QD Hybrid Architectures. *Small* **2019**, *15*, 1901606. [CrossRef]

16. Surre, F.; Bernal, O.D.; Seat, H.C.; Sharp, J.H. Estimation of Transition Metal Nitride Surface Plasmon Refractometer Sensitivity. In Proceedings of the IEEE Sensors, Montorel, QC, Canada, 27–30 October 2019.

17. Liu, J.; Guler, U.; Lagutchev, A.; Kildishev, A.; Malis, O.; Boltasseva, A.; Shalaev, V.M. Quasi-coherent thermal emitter based on refractory plasmonic materials. *Opt. Mater. Express* **2015**, *5*, 2721. [CrossRef]

18. Cao, Y.Q.; Zhao, X.R.; Chen, J.; Zhang, W.; Li, M.; Zhu, L.; Zhang, X.J.; Wu, D.; Li, A.D. TiOxNy Modified TiO$_2$ Powders Prepared by Plasma Enhanced Atomic Layer Deposition for Highly Visible Light Photocatalysis. *Sci. Rep.* **2018**, *8*, 1–9. [CrossRef]

19. Li, C.; Yang, W.; Li, Q. TiO$_2$-based photocatalysts prepared by oxidation of TiN nanoparticles and their photocatalytic activities under visible light illumination. *J. Mater. Sci. Technol.* **2018**, *34*, 969–975. [CrossRef]

20. Yuan, Y.; Wang, J.; Adimi, S.; Shen, H.; Thomas, T.; Ma, R.; Attfield, J.P.; Yang, M. Zirconium nitride catalysts surpass platinum for oxygen reduction. *Nat. Mater.* **2019**, *19*, 282–286. [CrossRef]

21. Awad, M.A.; Aly, A.H. Experimental and theoretical studies of hybrid multifunctional TiO$_2$/TiN/TiO$_2$. *Ceram. Int.* **2019**, *45*, 19036–19043. [CrossRef]

22. Li, G.; Zhang, P.; Bian, Z.; Zhu, J.; Wu, L.; Li, H. Mesoporous TiN microspheres with hierarchical chambers and enhanced visible light-driven hydrogen evolution. *ChemSusChem* **2013**, *6*, 1461–1466. [CrossRef]

23. Kumar, R.; Pasupathi, S.; Pollet, B.G.; Scott, K. Nafion-stabilised platinum nanoparticles supported on titaniumnitride: An efficient and durable electrocatalyst for phosphoric acidbased polymer electrolyte fuel cells. *Electrochim. Acta* **2013**, *109*, 365–369. [CrossRef]

24. Rabia, M.; Mohamed, S.H.; Zhao, H.; Shaban, M.; Lei, Y.; Ahmed, A.M. TiO2/TiOxNY hollow mushrooms-like nanocomposite photoanode for hydrogen electrogeneration. *J. Porous Mater.* **2020**, *27*, 133–139. [CrossRef]

25. Noothongkaew, S.; Thumthan, O.; An, K.S. Minimal layer graphene/TiO2 nanotube membranes used for enhancement of UV photodetectors. *Mater. Lett.* **2018**, *218*, 274–279. [CrossRef]

26. Wang, L.; Yang, W.; Chong, H.; Wang, L.; Gao, F.; Tian, L.; Yang, Z. Efficient ultraviolet photodetectors based on TiO$_2$ nanotube arrays with tailored structures. *RSC Adv.* **2015**, *5*, 52388–52394. [CrossRef]

27. Lee, Y.B.; Han, J.K.; Noothongkaew, S.; Kim, S.K.; Song, W.; Myung, S.; Lee, S.S.; Lim, J.; Bu, S.D.; An, K.-S. Toward Arbitrary-Direction Energy Harvesting through Flexible Piezoelectric Nanogenerators Using Perovskite PbTiO$_3$ Nanotube Arrays. *Adv. Mater.* **2017**, *29*, 1604500. [CrossRef]

28. Liu, G.; Karuturi, S.K.; Chen, H.; Wang, D.; Ager, J.W.; Simonov, A.N.; Tricoli, A. Enhancement of the photoelectrochemical water splitting by perovskite BiFeO$_3$ via interfacial engineering. *Sol. Energy* **2020**, *202*, 198–203. [CrossRef]

29. Abukhadra, M.R.; Rabia, M.; Shaban, M.; Verpoort, F. Heulandite/polyaniline hybrid composite for efficient removal of acidic dye from water; kinetic, equilibrium studies and statistical optimization. *Adv. Powder Technol.* **2018**, *29*, 2501–2511. [CrossRef]

30. Ahmed, A.M.; Rabia, M.; Shaban, M. The structure and photoelectrochemical activity of Cr-doped PbS thin films grown by chemical bath deposition. *RSC Adv.* **2020**, *10*, 14458–14470. [CrossRef]

31. Sherman, B.D.; Ashford, D.L.; Lapides, A.M.; Sheridan, M.V.; Wee, K.R.; Meyer, T.J. Light-Driven Water Splitting with a Molecular Electroassembly-Based Core/Shell Photoanode. *J. Phys. Chem. Lett.* **2015**, *6*, 3213–3217. [CrossRef]

32. Ahmed, A.M.; Shaban, M. Nanoporous chromium thin film for active detection of toxic heavy metals traces using surface-enhanced Raman spectroscopy. *Mater. Res. Express* **2020**, *7*, 1–8. [CrossRef]

33. Mohamed, S.H.; Zhao, H.; Romanus, H.; El-Hossary, F.M.; Abo EL-Kassem, M.; Awad, M.A.; Rabia, M.; Lei, Y. Optical, water splitting and wettability of titanium nitride/titanium oxynitride bilayer films for hydrogen generation and solar cells applications. *Mater. Sci. Semicond. Process.* **2020**, *105*, 104704. [CrossRef]

34. Sayyah, S.M.; Shaban, M.; Rabia, M. A sensor of m-toluidine/m-cresol polymer film for detection of lead ions by potentiometric methods. *Sens. Lett.* **2016**, *14*, 522–529. [CrossRef]

35. Sayyah, E.-S.M.; Shaban, M.; Rabia, M. A sensor of *m*-cresol nanopolymer/Pt-electrode film for detection of lead ions by potentiometric methods. *Adv. Polym. Technol.* **2018**, *37*, 1296–1304. [CrossRef]

36. Mohamed, F.; Rabia, M.; Shaban, M. Synthesis and characterization of biogenic iron oxides of different nanomorphologies from pomegranate peels for efficient solar hydrogen production. *J. Mater. Res. Technol.* **2020**, *9*, 4255–4271. [CrossRef]

37. Sharma, S.; Kumar, D.; Khare, N. Plasmonic Ag nanoparticles decorated Bi2S3 nanorods and nanoflowers: Their comparative assessment for photoelectrochemical water splitting. *Int. J. Hydrogen Energy* **2019**, *44*, 3538–3552. [CrossRef]

38. Zayed, M.; Ahmed, A.M.; Shaban, M. Synthesis and characterization of nanoporous ZnO and Pt/ZnO thin films for dye degradation and water splitting applications. *Int. J. Hydrogen Energy* **2019**, *44*, 17630–17648. [CrossRef]

39. Yang, L.; Liu, Z. Study on light intensity in the process of photocatalytic degradation of indoor gaseous formaldehyde for saving energy. *Energy Convers. Manag.* **2007**, *48*, 882–889. [CrossRef]

40. Sayyah, S.M.; Shaban, M.; Rabia, M. Electropolymerization of *m*-Toluidin on Platinum Electrode from Aqueous Acidic Solution and Character of the Obtained Polymer. *Adv. Polym. Technol.* **2018**, *37*, 126–136. [CrossRef]

41. Baniasadi, E.; Dincer, I.; Naterer, G.F. Measured effects of light intensity and catalyst concentration on photocatalytic hydrogen and oxygen production with zinc sulfide suspensions. *Int. J. Hydrogen Energy* **2013**, *38*, 9158–9168. [CrossRef]

42. Sayyah, S.M.; Shaban, M.; Rabia, M. A High-Sensitivity Potentiometric Mercuric Ion Sensor Based on m-Toluidine Films. *IEEE Sens. J.* **2016**, *16*, 1541–1548. [CrossRef]

43. Bell, S.; Will, G.; Bell, J. Light intensity effects on photocatalytic water splitting with a titania catalyst. *Int. J. Hydrogen Energy* **2013**, *38*, 6938–6947. [CrossRef]

44. Shaban, M.; Ahmed, A.M.; Abdel-Rahman, E.; Hamdy, H. Tunability and Sensing Properties of Plasmonic/1D Photonic Crystal. *Sci. Rep.* **2017**, *7*, 1–10. [CrossRef] [PubMed]

45. Razek, S.A.; Popeil, M.R.; Wangoh, L.; Rana, J.; Suwandaratne, N.; Andrews, J.L.; Watson, D.F.; Banerjee, S.; Piper, L.F.J. Designing catalysts for water splitting based on electronic structure considerations. *Electron. Struct.* **2020**, *2*, 023001. [CrossRef]

46. Freeman, E.; Kumar, S.; Thomas, S.R.; Pickering, H.; Fermin, D.J.; Eslava, S. PrFeO₃ Photocathodes Prepared Through Spray Pyrolysis. *ChemElectroChem* **2020**, *7*, 1365–1372. [CrossRef]

47. Wang, Z.; Cao, D.; Wen, L.; Xu, R.; Obergfell, M.; Mi, Y.; Zhan, Z.; Nasori, N.; Demsar, J.; Lei, Y. Manipulation of charge transfer and transport in plasmonic-ferroelectric hybrids for photoelectrochemical applications. *Nat. Commun.* **2016**, *7*, 1–8. [CrossRef] [PubMed]

48. Zhu, Y.; Wang, D.; Huang, Q.; Du, J.; Sun, L.; Meyer, T.J. Stabilization of a molecular water oxidation catalyst on a dye−sensitized photoanode by a pyridyl anchor. *Nat. Commun.* **2020**, *11*, 4610. [CrossRef]

49. Xiao, X.; Engelbrekt, C.; Zhang, M.; Li, Z.; Ulstrup, J.; Zhang, J.; Si, P. A straight forward approach to electrodeposit tungsten disulfide/poly(3,4-ethylenedioxythiophene) composites onto nanoporous gold for the hydrogen evolution reaction. *Appl. Surf. Sci.* **2017**, *410*, 308–314. [CrossRef]

50. Modibane, K.D.; Waleng, N.J.; Ramohlola, K.E.; Maponya, T.C.; Monama, G.R.; Makgopa, K.; Hato, M.J. Poly(3-aminobenzoic acid) Decorated with Cobalt Zeolitic Benzimidazolate Framework for Electrochemical Production of Clean Hydrogen. *Polymers* **2020**, *12*, 1581. [CrossRef]

51. Elsayed, A.M.; Rabia, M.; Shaban, M.; Aly, A.H.; Ahmed, A.M. Preparation of hexagonal nanoporous Al₂O₃/TiO₂/TiN as a novel photodetector with high efficiency. *Sci. Rep.* **2021**, *11*, 17572. [CrossRef]

52. Shaban, M.; Ali, S.; Rabia, M. Design and application of nanoporous graphene oxide film for CO2, H2, and C2H2 gases sensing. *J. Mater. Res. Technol.* **2019**, *5*, 4510–4520. [CrossRef]

53. Arrhenius, S. Über die Dissociationswärme und den Einfluss der Temperatur auf den Dissociationsgrad der Elektrolyte. *Z. Phys. Chem.* **1889**, *4U*, 96–116. [CrossRef]

54. Helmy, A.; Rabia, M.; Shaban, M.; Ashraf, A.M.; Ahmed, S.; Ahmed, A.M. Graphite/rolled graphene oxide/carbon nanotube photoelectrode for water splitting of exhaust car solution. *Int. J. Energy Res.* **2020**, *44*, 7687–7697. [CrossRef]

55. Shaban, N.; Abukhadra, M.R.; Rabia, M.; Elkader, Y.; Abd El-Halim, M.R. Investigation the adsorption properties of graphene oxide and polyaniline nano/micro structures for efficient removal of toxic Cr(VI) contaminants from aqueous solutions; kinetic and equilibrium studies. *Rendiconti Lincei. Scienze Fisiche e Naturali* **2018**, *29*, 154. [CrossRef]

56. Shaban, M.; Rabia, M.; Eldakrory, M.G.; Maree, R.M.; Ahmed, A.M. Efficient photoselectrochemical hydrogen production utilizing of APbI3 (A = Na, Cs, and Li) perovskites nanorods. *Int. J. Energy Res.* **2020**, er.6326. [CrossRef]

57. Zaki, S.E.; Basyooni, M.A.; Shaban, M.; Rabia, M.; Eker, Y.R.; Attia, G.F.; Yilmaz, M.; Ahmed, A.M. Role of oxygen vacancies vanadium oxide and oxygen functional groups in graphene oxide for room temperature CO2 gas sensors. *Sens. Actuator A Phys.* **2019**, *294*, 17–24. [CrossRef]

58. Rabia, M.; Shaban, M.; Jibali, B.M.; Abdelkhaliek, A.A. Effect of Annealing Temperature on the Photoactivity of ITO/VO2 (M)/Au Film Electrodes for Water Splitting. *J. Nanosci. Nanotechnol.* **2020**, *20*, 4120–4130. [CrossRef]

59. Eyring, H. The activated complex in chemical reactions. *J. Chem. Phys.* **1935**, *3*, 63–71. [CrossRef]

60. Thompson, M.C.; Barad, B.A.; Wolff, A.M. Temperature-jump solution X-ray scattering reveals distinct motions in a dynamic enzyme. *Nat. Chem.* **2019**, *11*, 1058–1066. [CrossRef]

61. Mohamed, H.S.H.; Rabia, M.; Zhou, X.G.; Qin, X.S.; Khabiri, G.; Shaban, M.; Younus, H.A.; Taha, S.; Hu, Z.Y.; Liu, J.; et al. Phase-junction Ag/TiO2 nanocomposite as photocathode for H2 generation. *J. Mater. Sci. Technol.* **2021**, *83*, 179–187. [CrossRef]

62. Cannelli, Q.; Bacellar, C.; Ingle, R.A.; Bohinc, R.; Kinschel, D.; Bauer, B.; Ferreira, D.S.; Grolimund, D.; Mancini, G.F.; Cherqui, M. Toward time-resolved laser T-jump/X-ray probe spectroscopy in aqueous solutions. *Struct. Dyn.* **2019**, *6*, 064303. [CrossRef]

63. Mohamed, H.S.H.; Rabia, M.; Shaban, M.; Taha, S. Controlled synthesis of CdS nanoflowers thin films for H2 electro-generation. *Mater. Sci. Semicond. Process.* **2020**, *120*. [CrossRef]

64. Naldoni, A.; Guler, U.; Wang, Z.; Marelli, M.; Malara, F.; Meng, X.; Besteiro, L.V.; Govorov, A.O.; Kildishev, A.V.; Boltasseva, A.; et al. Broadband Hot-Electron Collection for Solar Water Splitting with Plasmonic Titanium Nitride. *Adv. Opt. Mater.* **2017**, *5*, 1601031. [CrossRef]

65. Hao, Q.; Wang, C.; Huang, H.; Li, W.; Du, D.; Han, D.; Qiu, T.; Chu, P.K. Aluminum plasmonic photocatalysis. *Sci. Rep.* **2015**, *5*, 1–7. [CrossRef]

66. Jiang, L.; Zhou, G.; Mi, J.; Wu, Z. Fabrication of visible-light-driven one-dimensional anatase TiO$_2$/Ag heterojunction plasmonic photocatalyst. *Catal. Commun.* **2012**, *24*, 48–51. [CrossRef]

67. Sellappan, R.; Nielsen, M.G.; González-Posada, F.; Vesborg, P.C.K.; Chorkendorff, I.; Chakarov, D. Effects of plasmon excitation on photocatalytic activity of Ag/TiO$_2$ and Au/TiO$_2$ nanocomposites. *J. Catal.* **2013**, *307*, 214–221. [CrossRef]

68. Langhammer, C.; Schwind, M.; Kasemo, B.; Zorić, I. Localized Surface Plasmon Resonances in Aluminum Nanodisks. *Nano Lett.* **2008**, *8*, 1461–1471. [CrossRef] [PubMed]

69. Long, R.; Prezhdo, O.V. Instantaneous Generation of Charge-Separated State on TiO2 Surface Sensitized with Plasmonic Nanoparticles. *J. Am. Chem. Soc.* **2014**, *136*, 4343–4354. [CrossRef]

70. Christopher, P.; Ingram, D.B.; Linic, S. Enhancing photochemical activity of semiconductor nanoparticles with optically active Ag nanostructures: Photochemistry mediated by Ag surface plasmons. *J. Phys. Chem. C* **2010**, *114*, 9173–9177. [CrossRef]

71. Ingram, D.B.; Linic, S. Water splitting on composite plasmonic-metal/semiconductor photoelectrodes: Evidence for selective plasmon-induced formation of charge carriers near the semiconductor surface. *J. Am. Chem. Soc.* **2011**, *133*, 5202–5205. [CrossRef]

72. Guler, U.; Shalaev, V.M.; Boltasseva, A. Nanoparticle plasmonics: Going practical with transition metal nitrides. *Mater. Today* **2015**, *18*, 227–237. [CrossRef]

73. Yick, S.; Murdock, A.T.; Martin, P.J.; Kennedy, D.F.; Maschmeyer, T.; Bendavid, A. Tuning the plasmonic response of TiN nanoparticles synthesised by the transferred arc plasma technique. *Nanoscale* **2018**, *10*, 7566–7574. [CrossRef] [PubMed]

74. Fillot, F.; Morel, T.; Minoret, S.; Matko, I.; Maîtrejean, S.; Guillaumot, B.; Chenevier, B.; Billon, T. Investigations of titanium nitride as metal gate material, elaborated by metal organic atomic layer deposition using TDMAT and NH3. *Microelectron. Eng.* **2005**, *82*, 248–253. [CrossRef]